

Extremely High Excitation SiO Lines in Disk-Outflow System in Orion Source I

Mi Kyoung Kim^{1,2}, Tomoya Hirota^{3,4}, Masahiro N. Machida⁵, Yuko Matsushita⁵, Kazuhito Motogi⁶, Naoko Matsumoto^{3,7} & Mareki Honma^{1,8}

mikyoung.kim@nao.ac.jp

ABSTRACT

We present high-resolution images of the submillimeter SiO line emissions of a massive young stellar object Orion Source I using the Atacama Large Millimeter/Submillimeter Array (ALMA) at band 8. We detected the 464 GHz SiO $v=4$ $J=11-10$ line in Source I, which is the first detection of the SiO $v=4$ line in star-forming regions, together with the 465 GHz ^{29}SiO $v=2$ $J=11-10$ and the 428 GHz SiO $v=2$ $J=10-9$ lines with a resolution of 50 AU. The ^{29}SiO $v=2$ $J=11-10$ and SiO $v=4$ $J=11-10$ lines have compact structures with the diameter of <80 AU. The spatial and velocity distribution suggest that the line emissions are associated with the base of the outflow and the surface of the edge-on disk. In contrast, SiO $v=2$ $J=10-9$ emission shows a bipolar structure in the direction of northeast-southwest low-velocity outflow with ~ 200 AU scale. The emission line exhibits a velocity gradient along the direction of the disk elongation. With the assumption of the ring structure with Keplerian rotation, we estimated the lower limit of the central mass to be $7 M_{\odot}$ and the radius of $12 \text{ AU} < r < 26 \text{ AU}$.

¹Mizusawa VLBI Observatory, National Astronomical Observatory of Japan, Hoshigaoka 2-12, Mizusawa-ku, Oshu, Iwate 023-0861, Japan

²Korea Astronomy and Space Science Institute, Hwaam-dong 61-1, Yuseong-gu, Daejeon, 305-348, Republic of Korea

³Mizusawa VLBI Observatory, National Astronomical Observatory of Japan, Osawa 2-21-1, Mitaka, Tokyo 181-8588, Japan

⁴Department of Astronomical Sciences, SOKENDAI (The Graduate University for Advanced Studies), Osawa 2-21-1, Mitaka, Tokyo 181-8588, Japan

⁵Department of Earth and Planetary Sciences, Faculty of Sciences, Kyushu University, Motooka 744, Nishi-ku, Fukuoka, Fukuoka 819-0395, Japan

⁶Graduate School of Science and Engineering, Yamaguchi University, Yoshida 1677-1, Yamaguchi, Yamaguchi 753-8511, Japan

⁷The Research Institute for Time Studies, Yamaguchi University, Yoshida 1677-1, Yamaguchi, Yamaguchi 753-8511, Japan

⁸Department of Astronomical Sciences, SOKENDAI (The Graduate University for Advanced Studies), Hoshigaoka2-12, Mizusawa-ku, Oshu, Iwate 023-0861, Japan

Subject headings: ISM: individual objects (Orion KL) — radio continuum: stars — stars: formation — stars: individual (Orion Source I)

1. Introduction

Orion Source I is a high-mass protostar candidate located in the Orion KL (Kleinmann-Low) region (Kleinmann & Low 1967). Source I is thought to have a high-luminosity of $>10^4 L_{\odot}$, however, it is so highly embedded that cannot be observed directly at optical and infrared wavelengths. Due to its proximity ($D \sim 420$ pc) (Menten et al. 2007; Hirota et al. 2007; Kim et al. 2008), Source I has been studied in detail via the high-resolution observations with radio and sub-mm wavelengths.

The source is associated with a low-velocity ($V \sim 18$ km s $^{-1}$) bipolar outflow with a size of ~ 1000 AU along the northeast-southwest direction (Plambeck et al. 2009; Zapata et al. 2012; Greenhill et al. 2013). The radio continuum observations with Very Large Array (VLA) and ALMA have imaged the elongated continuum emission at the center of the outflow, which is consistent with an edge-on disk perpendicular to the bipolar outflow (Reid et al. 2007; Goddi et al. 2011; Hirota et al. 2015; Plambeck & Wright 2016; Orozco-Aquilara et al. 2017). The bright SiO maser emission, which is rare in the star-forming regions, has been found toward Source I. The high-resolution observations with VLBI revealed that the 43 GHz $v=1$ and 2 $J=1-0$ SiO maser spots are distributed in X-shaped region with a size of ~ 100 AU (Greenhill et al. 1998; Kim et al. 2008; Matthews et al. 2010; Issaoun et al. 2017). The observations revealed that the masers have a stable velocity gradient in the direction parallel the elongation of the radio continuum, while moving outward along the arms of X-shape. These behaviors suggest that the masers are associated with the rotating outflow from the surface of the disk. Recent ALMA observations detected high-frequency lines of H $_2$ O, CO, and silicon- and sulfur-rich molecules at the position of Source I (e.g. Hirota et al. 2012, 2014, 2016a, 2017; Plambeck & Wright 2016; Ginsburg et al. 2018), which are tracing the disk and the outflowing gas from the disk. The velocity structure of the high-frequency lines also shows the rotational feature similar to those of the 43 GHz $v=1$ and 2 SiO masers. The observed velocity gradients can be modeled with Keplerian rotation curve with the enclosed mass of $\sim 5-9 M_{\odot}$ (Matthews et al. 2010; Kim et al. 2008; Hirota et al. 2014; Plambeck & Wright 2016; Hirota et al. 2017). More recently, Ginsburg et al. (2018) reported the continuum and spectral line emission from Source I's disk and outflow with ALMA observation at a resolution of 0.03-0.06". They detected the continuum and several unidentified line emission in the disk, as well as thermal H $_2$ O $5_{5,0}-6_{4,3}$ line tracing upper and lower boundary of the disk. The kinematics and morphology of the continuum and line emission confirmed the idea of rotating outflow from the disk suggested in the previous studies, although they obtained the higher central mass of $\sim 15 M_{\odot}$.

The high-resolution observations of the masers and the high-frequency line emissions reveal a rotating, wide-angle inner outflow and a perpendicular disk around Source I, which can be explained

by magneto-centrifugal disk wind launched by the central high-mass young stellar object (e.g. Matthews et al. 2010; Greenhill et al. 2013; Hirota et al. 2017). This picture is similar to the the low-mass star formation scenario, which describes the transfer of mass and angular momentum between the accretion disk and outflows (Hirota et al. 2017; Vaidya & Goddi 2013). Besides, the ALMA observations with CH_3CN and CH_3OH lines revealed the signature of the infall motion toward Source I, which also supports the star formation via accretion (Wu et al. 2014). On the other hand, the proper motion measurements of young stellar objects in Orion KL suggested that dynamical interactions between massive stars played a role in the evolution of Source I (Rodríguez et al. 2005; Bally et al. 2011; Goddi et al. 2011; Rodríguez et al. 2017). The scenarios suggest that the dynamical decay of a multiple-star system consist of BN, Source I and perhaps source n occurred ~ 500 years ago, and released gravitational energy during the interaction would have triggered the explosive outflow seen in H_2 and CO. The scenarios expect the Source I to be $\sim 20 M_\odot$ binary system (Goddi et al. 2011; Bally et al. 2011; Rodríguez et al. 2017). The mass of Source I reported by Ginsburg et al. (2018) of $15M_\odot$ is more consistent with these scenarios than those of previous values, although there are still controversies in the detailed process (Chatterjee & Tan 2012; Luhman et al. 2017).

The study of the physical properties of Source I requires the information of inner outflow/disk region with higher resolution observations. Toward this goal, the high-excitation transition lines could be a potential tool to investigate the hot and dense gas near the protostar (Hirota et al. 2014, 2017; Plambeck & Wright 2016; Ginsburg et al. 2018). In this paper, we present the results of ALMA observations at $0.1''$ resolution to study dynamical properties of the disk-outflow system in the close vicinity to Source I. The observation yields the maps of SiO lines with the excitation temperature of 3600-7000 K, which trace the inner part of the disk-outflow system of Source I.

2. Observations

Observations were executed on August 27 (460 GHz), and September 22 (430 GHz) in 2015 with the Atacama Large Millimeter/Submillimeter Array (ALMA) as one of the science projects in cycle 2 (ADS/JAO.ALMA#2013.1.00048.S). Details of observations are summarized in Hirota et al. (2016b, 2017). The tracking center position of the target source was $\text{RA}(\text{J2000})=05\text{h}35\text{m}14.512\text{s}$, $\text{Decl}(\text{J2000})=-05^\circ22'30.57''$. The total on-source integration times of the target source were 458 seconds, and 2065 seconds for 460 GHz, and 430 GHz, respectively. The line information presented in this paper are summarized in Table 1. For the observations at both 430 and 460 GHz, a primary flux calibrator was J0423–013, and a band-pass calibrator was J0522–3627. The secondary gain calibrators were J0607–0834 for 460 GHz observations and J0501-0159 for 430 GHz observations. The array was composed of 40 and 35 antennas with the maximum baseline length of 1575 m and 2270 m at 460 GHz and 430 GHz, respectively. The average system noise temperature was ~ 300 K at 460 GHz and 500 K at 430 GHz. The spectral window centered at 428.0 GHz and 464.6 GHz included observed SiO line emissions. The total bandwidth of the spectral bands

was 1875 MHz, and the channel spacing was 976.562 kHz, corresponding the velocity resolution of $\sim 0.6 \text{ km s}^{-1}$.

The self-calibration and the synthesized imaging were carried out using the CASA software package. The details of the data analysis are summarized in Hirota et al. (2016b, 2017). The synthesized images of each velocity channels were made for all lines by using the CASA task `clean` with uniform-weighting. The synthesized beam sizes were $0.13'' \times 0.11''$ with the position angle of 82° for the 465 GHz $^{29}\text{SiO } v=2 J=11-10$ line, $0.12'' \times 0.11''$ with the position angle of 87° for the 464 GHz SiO $v=4 J=11-10$ line, and $0.09'' \times 0.07''$ with the position angle of 82° for the 428 GHz SiO $v=2 J=10-9$ line. We made the moment maps using the CASA task `immoments`. To make a position centroid maps of the line emission, we did a two-dimensional Gaussian fitting to each velocity channel maps using the task `JMFIT` with the AIPS software package. As discussed in Hirota et al. (2016b), the continuum peak positions at different frequencies deviate from each other by 100 mas at maximum for astrometric calibration errors in the observations or data analysis. Thus, we did not use the absolute position of the emissions in comparing the maps at different frequency bands in this paper.

3. Results

3.1. Spectral profile

We successfully detected 465 GHz $^{29}\text{SiO } v=2 J=11-10$, 464 GHz SiO $v=4 J=11-10$, and 428 GHz SiO $v=2 J=10-9$ lines toward Source I. Especially, this is the first time to detect the SiO $v=4 J=11-10$ line in star-forming regions. The SiO $v=4$ transition has been detected toward a red supergiant VY CMa at $J=5-4$ transition at 211 GHz for the first time (Cernicharo et al. 1993). Recently, owing to the high spectral resolution and the sensitivity of ALMA, SiO emission with the higher vibrational excitation level has been observed in late-type stars (Decin et al. 2018; Kervella

Table 1. Observed lines

Frequency (MHz)	Molecule	Transition	E_l (K)
465014.010	^{29}SiO	$v=2, 11-10$	3611
428087.451	SiO	$v=2, 10-9$	3614
464244.956	SiO	$v=4, 11-10$	7086

Note. — ine information are taken from the Cologne Database for Molecular Spectroscopy (CDMS) (Müller et al. 2005). E_l is the lower state energy.

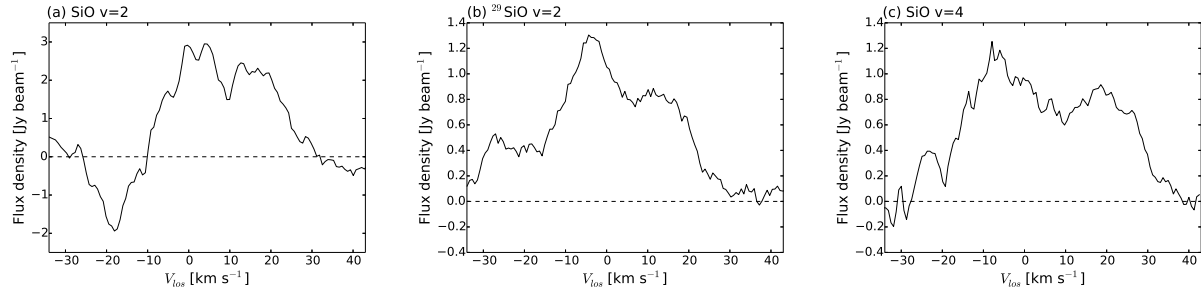


Fig. 1.— The spectra of the observed SiO lines summed over 0.24×0.24 arcsec. Horizontal dashed lines mark the baseline. (a) The spectrum of the SiO $v=2$ $J=10-9$ line emission. (b) The spectrum of the ^{29}SiO $v=2$ $J=11-10$ line emission. (c) The spectrum of the SiO $v=4$ $J=11-10$ line emission.

et al. 2018). Decin et al. (2018) detected the SiO $v=4$ and 5 $J=8-7$ line (R Dor and IK Tau) and Si ^{18}O $v=5$ $J=9-8$ (IK Tau) in AGB stars¹, and Kervella et al. (2018) observed the SiO $v=6$ and 7 $J=8-7$ line in a red supergiant Betelgeuse.

Figure 1 displays the observed SiO line spectra summed over $0.24'' \times 0.24''$ boxes centered on the continuum peaks. The velocities of the emissions range from ~ -30 km s^{-1} to ~ 30 km s^{-1} , and generally centered on $V_{lsr} \sim 5$ km s^{-1} , which is the systemic velocity of Source I (Plambeck et al. 1990). The ^{29}SiO $v=2$ $J=11-10$ and SiO $v=4$ $J=11-10$ emission show double peak profiles with the peak velocities at ~ -5 km s^{-1} and ~ 15 km s^{-1} , which are similar to those of other high-frequency lines and masers (Kim et al. 2008; Hirota et al. 2012; Matthews et al. 2010; Greenhill et al. 2013; Hirota et al. 2014, 2016a, 2017; Ginsburg et al. 2018).

The SiO $v=2$ $J=10-9$ line spectrum also shows the double peak profile, but the velocity of the blue-shifted emission peak is shifted by $\sim 5-10$ km s^{-1} from those of other emission lines. Also, the SiO $v=2$ $J=10-9$ line appears in absorption at the velocity range of $-25 < V_{lsr} < -10$ km s^{-1} . It is unlikely to be explained by a self-absorption because the SiO $v=2$ $J=10-9$ line has a high excitation temperature of $E_l \sim 3600$ K and they would be located very close to the central star. A possible candidate for the absorption line is the SO $v=0$ $9_{10} - 8_9$ at 428110.747 MHz ($E_l = 100$ K), which has a velocity of ~ -1 km s^{-1} at the absorption peak. In Orion-KL, SO emission is detected in the hot core and the compact ridge gas, as well as the disk and outflow near Source I (Plambeck & Wright 2016; Wright et al. 1996). However, the velocity of the gas in the hot core and the compact ridge is 2-11 km s^{-1} . Thus, the absorption is likely to be associated with the SO in the outflow. Plambeck & Wright (2016) also reported the asymmetric absorption limited to blue-shifted velocities ($-13 < V_{lsr} < 5$ km s^{-1}) in molecular lines with upper state energies $E_U < 500$ K, especially in the sulfur-bearing species. They also suggested that the absorption could be associated with material within the outflow of Source I because the velocity width of the absorption corresponds to the halfwidth of other lines associated with the outflow.

3.2. Spatial structure

Figure 2 displays the integrated intensity and peak velocity maps of SiO emissions overlaid with the continuum emission at 430 GHz and 460 GHz. In Figure 2 (b) and (c), $^{29}\text{SiO } v=2 J=11-10$ and SiO $v=4 J=11-10$ emissions exhibit the compact structures centered on Source I with the deconvolved size of $0.13'' \times 0.13''$ and $0.08'' \times 0.06''$, respectively. Both lines show the velocity gradient along the northwest-southeast direction, which is similar with $v=1$ and $2 J=1-0$ SiO masers (Matthews et al. 2010; Kim et al. 2008) and H_2O emission (Hirota et al. 2014, 2017). It is clear that the $v=4$ transition with the highest excitation energy level arises at the smallest radii from the YSO, where high temperatures are expected. In contrast to the elongated structure of the continuum emission, the $^{29}\text{SiO } v=2 J=11-10$ and SiO $v=4 J=11-10$ emission show almost circular structure. Besides, it seems that the peak positions of the both SiO lines slightly offset to the northeast direction from the peak position of the continuum emission. This result is consistent with the previous ALMA observations reporting that the molecular line emission offset from the disk midplane (Ginsburg et al. 2018; Plambeck & Wright 2016). Plambeck & Wright (2016) reported that line emissions such as SiS are spatially extended relative to the continuum. Also, Ginsburg et al. (2018) separated the line emitting region from the continuum emission with higher angular resolution and reported that the SiO and H_2O lines are seen in the region below and above the continuum emission. It suggests the continuum emission is most likely optically thick emission from the disk, and molecular line emissions originate from the atmosphere of the disk and/or the base of the outflow.

The peak flux densities of $^{29}\text{SiO } v=2 J=11-10$ and SiO $v=4 J=11-10$ lines are 1.3 Jy and 1.2 Jy at the LSR velocity of -4.3 km s^{-1} and -6 km s^{-1} , respectively. We measured the source size of each channel as $0.2'' \times 0.16''$ and $0.15'' \times 0.13''$ with the two-dimensional Gaussian fitting to the channel maps. Using measured flux densities and the source sizes, the brightness temperatures of $^{29}\text{SiO } v=2 J=11-10$ and SiO $v=4 J=11-10$ lines are estimated to be 229 K and 349 K. The estimated brightness temperatures are lower than the temperature of the dust (500-800 K) and the gas (1000-2000 K) (Hirota et al. 2016b; Plambeck & Wright 2016; Goddi et al. 2009). One of the possible explanations is that SiO lines are optically thin thermal emission.

On the other hand, we cannot exclude the possibility of the maser nature of $^{29}\text{SiO } v=2 J=11-10$ and SiO $v=4 J=11-10$ lines because of the similarity with other maser transitions, such as the small distribution comparable to the 43 GHz $v=1, 2 J=1-0$ masers, and the high density/temperature in this region. From the spectral energy distribution, Plambeck & Wright (2016) inferred the disk mass of $0.02-0.2M_\odot$ and the $n_H > 3.2 \times 10^{10} \text{ cm}^{-3}$. The existence of SiO $v=1$ and $2 J=1-0$ masers also suggest that the temperature and the density at the disk surface must be 1000-2000 K and $10^{10 \pm 1} \text{ cm}^{-3}$ (Goddi et al. 2009).

In the model calculation for the excitation of SiO $v=4 J=5-4$ maser presented for VY CMa (Cernicharo et al. 1993), the pumping of the SiO $v=4$ maser requires the local density of $\sim 0.5-5 \times 10^{10} \text{ cm}^{-3}$ at the gas temperature of 1500 K. Although the physical properties of the SiO maser

emitting region in a late-type star would be different from those in Source I, the disk properties of Source I is hot and dense enough to pump even $v=4$ SiO maser. In this case, the estimated brightness temperature of 229 K and 349 K would be the lower limits considering the possibility that the compact maser emission is unresolved.

In Figure 2 (a), the SiO $v=2$ $J=10-9$ emission exhibits a bipolar structure centered on Source I a size of $\sim 0.5'' \times 0.5''$, which is also visible in images of the low-velocity northeast-southwest outflow traced by SiO and H₂O lines including several maser lines (e.g., Plambeck et al. 2009; Niederhofer et al. 2012; Greenhill et al. 2013; Hirota et al. 2017). The moment 1 map clearly shows the velocity gradient in the northwest-southeast direction, and it is consistent with that of outflow with the size of $< 5''$ (Kim et al. 2008; Greenhill et al. 2013; Hirota et al. 2017). The moment 0 map indicates that the redshifted emission of the SiO $v=2$ $J=10-9$ line is dominant over the blue-shifted emission. This trend is also seen in 658 GHz and 321 GHz H₂O line (Hirota et al. 2014, 2016a), which trace the base of the outflow from the rotation disk around Source I. We confirmed that the absorption of the blue-shifted emission is located at the southeast part of the bipolar structure. It supports the idea that the material within the outflow or the disk of Source I result in the absorption feature (Plambeck & Wright 2016).

4. Discussion

4.1. Comparison with SiO $v=1$ and 2 $J=1-0$ masers

Our results show that the size of the spatial distributions and the velocity ranges of high-frequency SiO emission are consistent with those of SiO $v=1$ and 2 $J=1-0$ masers. To compare the distributions between the different SiO lines, we calculated the relative positions of SiO $v=1$ and 2 $J=1-0$ masers towards the position of Source I using the absolute positions measured by Kim et al. (2008) and Goddi et al. (2011). Then, we overlaid the maps registering the peak position of the continuum emissions to the position of Source I. Figure 2 (a) shows the positions of the $v=1$ and 2 $J=1-0$ SiO masers superposed on the moment map of SiO $v=2$ $J=10-9$ line and the 430 GHz continuum emission. It reveals that the X-shaped distribution of SiO $v=1$ and 2 $J=1-0$ masers are well consistent with the base of the bipolar structure of SiO $v=2$ $J=10-9$ emission, as well as the upper and lower boundary of the continuum emission. This result confirms the idea that the SiO $v=2$ $J=10-9$ line traces the base of rotating outflow driven by the magneto-centrifugal disk wind launched by a central star (Hirota et al. 2017).

To evaluate the detailed structure of SiO $v=4$ $J=11-10$ and ²⁹SiO $v=2$ $J=11-10$ emission, we made position centroid maps by performing two-dimensional Gaussian fitting to each velocity channel maps. Figure 3 displays the position centroids of $v=1$ and 2 $J=1-0$ SiO maser, SiO $v=4$, and ²⁹SiO $v=2$ $J=11-10$ emissions. With the synthesized beam size and SNR at the peak velocity channel of each line, the positional accuracy was as high as ~ 1 mas for the $v=4$ $J=11-10$ line and ~ 2 mas for the $v=2$ $J=11-10$ line. The results demonstrate the offset of $v=4$ $J=11-10$ line and

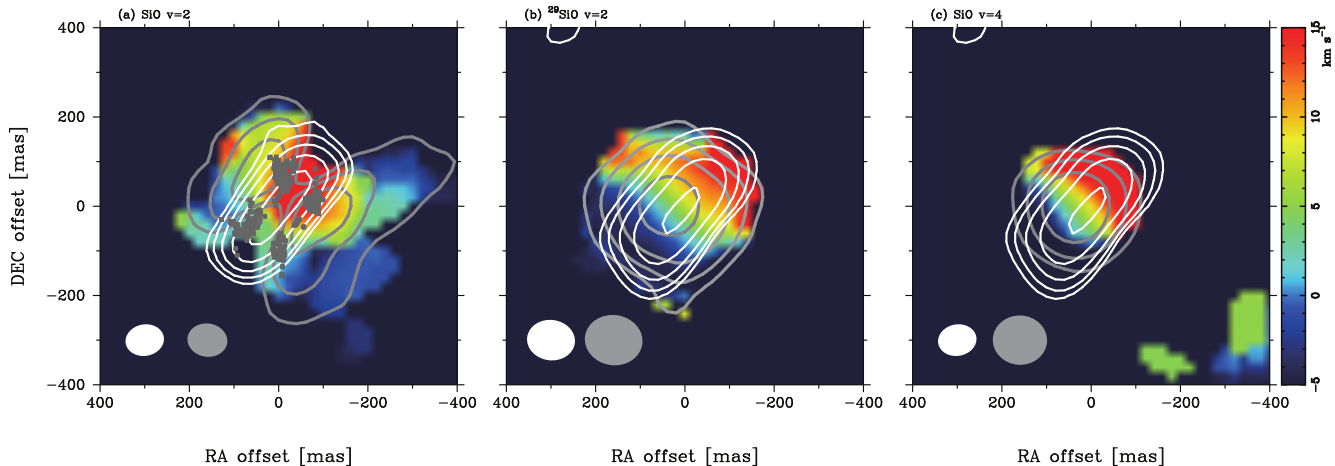


Fig. 2.— Moment 0 (grey contour) and moment 1 maps (color) of observed SiO lines superposed on the continuum map (white contour). The contour levels are 5, 10, 20, 40, and 80 times root-mean-square (RMS) noise levels, and the RMS noise levels are 3 mJy beam⁻¹ and 5 mJy beam⁻¹, respectively, for 430 GHz and 460 GHz continuum maps. (a) Map of SiO $v=2$ $J=10-9$ and 430 GHz continuum emission. The contour levels are 5, 10, and 20 times RMS noise level of 26 mJy beam⁻¹ for SiO $v=2$ $J=10-9$ line. Grey dots represent the position of SiO $v=1$ and 2 $J=1-0$ maser emission (Kim et al. 2008). The beam sizes are $0.09'' \times 0.07''$ (grey ellipse), PA=82° and $0.08'' \times 0.07''$ (white ellipse), PA=-80° for SiO $v=2$ $J=10-9$ and 430 GHz continuum emission, respectively. (b) Map of ²⁹SiO $v=2$ $J=11-10$ and 460 GHz continuum emission. The contour levels are 5, 10, 20, and 40 times RMS noise level of 33 mJy beam⁻¹ for ²⁹SiO $v=2$ $J=11-10$ line. The beam sizes are $0.13'' \times 0.11''$, PA=82° (grey ellipse) and $0.10'' \times 0.09''$, PA=83° (white ellipse) for ²⁹SiO $v=2$ $J=11-10$ and 460 GHz continuum emission, respectively. (c) Map of SiO $v=4$ $J=11-10$ and 460 GHz continuum emission. The contour levels are 5, 10, and 20 times RMS noise level of 57 mJy beam⁻¹ for SiO $v=4$ $J=11-10$ line. The beam sizes are $0.12'' \times 0.11''$, PA=87° (grey ellipse) and $0.10'' \times 0.09''$, PA=83° (white ellipse) for SiO $v=4$ $J=11-10$ and 460 GHz continuum emission, respectively.

²⁹SiO $v=2$ $J=11-10$ emissions from the disk midplane, as also seen in Section 3.2. While Ginsburg et al. (2018) resolved the molecular line emission from above and below the disk, we could not detect the emission in the southwest of the disk, possibly due to the lower sensitivity and resolution.

The ²⁹SiO $v=2$ $J=11-10$ emission is mainly found between the eastern and northern arms of X-shape, and also in the vertical structures from the disk, such as blue-shifted emission along the eastern arm and high-velocity components near the disk midplane. It confirms that the ²⁹SiO $v=2$ $J=11-10$ emission traces the rotating outflow as other SiO line emission (Plambeck & Wright 2016; Hirota et al. 2017; Ginsburg et al. 2018, e.g.). On the other hand, the $v=4$ $J=11-10$ emission only found in a line connecting the base of eastern and northern arms of 43 GHz SiO masers, which resembles the H₂O emission in Ginsburg et al. (2018). The morphology and velocity gradient of

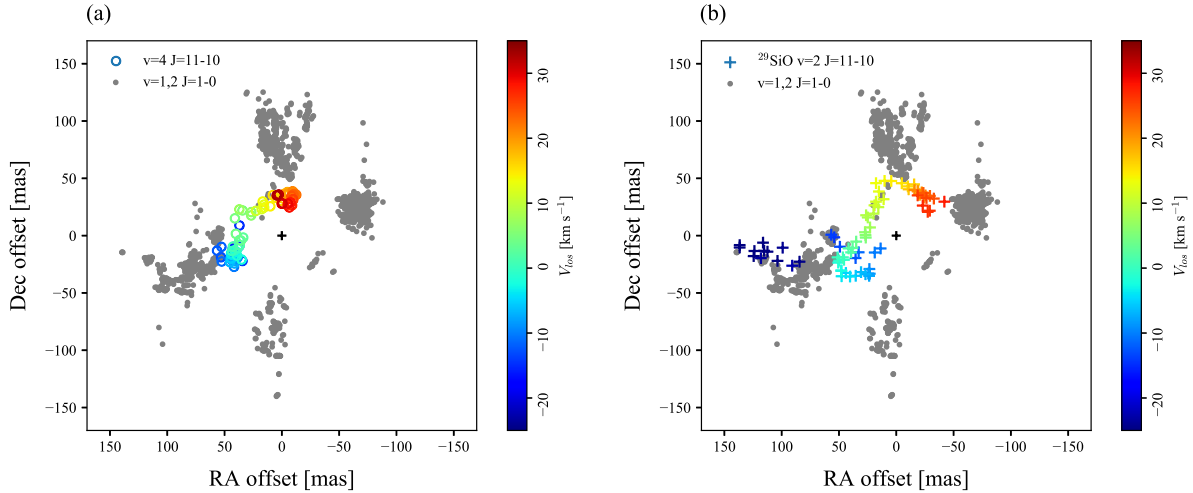


Fig. 3.— (a) The peak positions of the SiO $v=1$ and $2 J=1-0$ maser emission (grey circle) and the SiO $v=4 J=11-10$ emission (colored circle). (b) The peak positions of the SiO $v=1$ and $2 J=1-0$ maser emission (grey circle) and $^{29}\text{SiO } v=2 J=11-10$ emission (colored cross). The color of the SiO $v=4$ and $^{29}\text{SiO } v=2$ emission represents the line-of-sight velocity. The cross at $(0, 0)$ corresponds to the position of Source I (Goddi et al. 2011).

this line suggests that it traces both the surface of the disk and the base of the outflow.

4.2. The kinematics of $v=4 J=11-10$ line emission

Figure 4 shows the position-velocity diagrams of the SiO $v=4 J=11-10$ and $^{29}\text{SiO } v=2 J=11-10$ emission along the axis with the position angle of 140° (Hirota et al. 2014). The spatial distribution and the velocity gradients along the major axis of the continuum emission indicate that SiO $v=4 J=11-10$ emission is related to the rotating disk. However, the absence of the high-velocity components at the central position suggests that the high-frequency SiO line emissions are associated with a rotating ring structure rather than a filled disk. To find the parameters of the ring structure, we fit the observed rotation curve with a simulated rotation curve using a simple model similar to those of Hirota et al. (2014) and Plambeck & Wright (2016). We assumed a thin, edge-on ring structure in Keplerian rotation around a central star. In each position, the gas with uniform temperature and density emit the optically thin emission. The thermal width of 3 km s^{-1} was assumed. We set the systemic velocity of 6 km s^{-1} , which is the central value of the observed velocity range. We simulated the rotation curve for a range of inner radii r_{in} and outer radii r_{out} with the central masses ranges from 5 to $15 M_\odot$. As a result, we assess that $r_{in}=12 \text{ AU}$, $r_{out}=26 \text{ AU}$, and the central mass of $7 M_\odot$ for the best parameter.

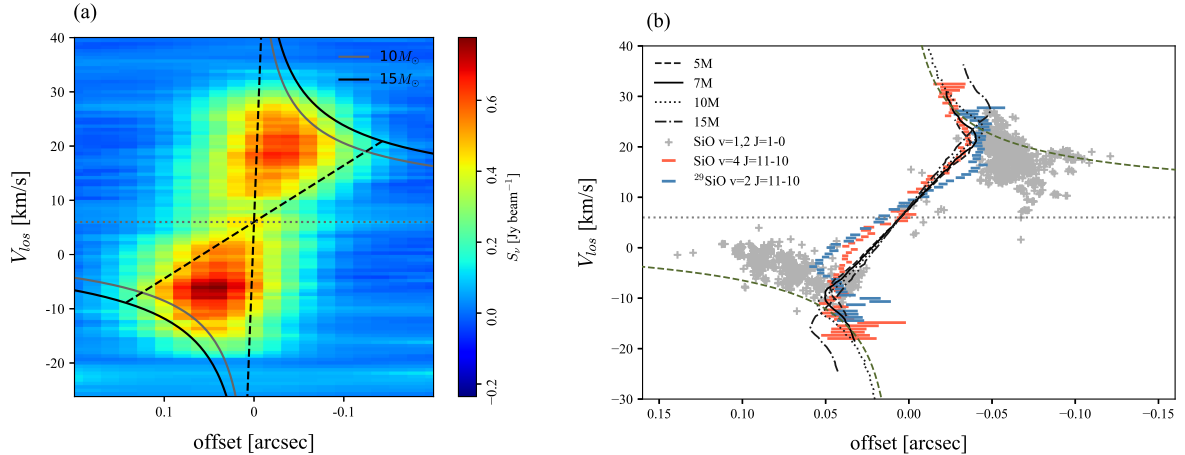


Fig. 4.— (a) The position-velocity diagram of the SiO $v=4$ $J=11-10$ emission. The Keplerian velocity curves for $10M_{\odot}$ (grey) and $15M_{\odot}$ (black) are overlaid. The dashed lines show the velocity curves at 5 AU and 60 AU. The dotted horizontal line represents the systemic velocity of 6 km s^{-1} . (b) The position-velocity diagram using the centroids of each velocity channel of the SiO $v=1$ and 2 $J=1-0$ SiO maser emission (grey cross), the $v=4$ $J=11-10$ (orange) and ^{29}SiO $v=2$ $J=11-10$ (blue) emission. The solid line indicates the position-velocity diagram of the ring model with parameters of $M = 7M_{\odot}$, $r_{in}=12 \text{ AU}$, $r_{out}=26 \text{ AU}$. Also, we overlaid the model curves with $M = 5M_{\odot}$ with $r_{in}=13 \text{ AU}$, $r_{out}=23 \text{ AU}$, $M = 10M_{\odot}$ with $r_{in}=6 \text{ AU}$, $r_{out}=30 \text{ AU}$, and $M = 15M_{\odot}$ with $r_{in}=16 \text{ AU}$, $r_{out}=30 \text{ AU}$. The dashed green line represents the Keplerian rotation curve with $M = 7M_{\odot}$. The horizontal dashed line marks the adopted systemic velocity of 6 km s^{-1} .

Figure 4 (b) presents the results of the fitting to the velocity centroids of the SiO $v=4$ $J=11-10$ emission. We also display the rotation curves with the central mass of 5, 10, and $15M_{\odot}$. The rotation curves for smaller masses also seems to fit with the observed rotation curve near the systematic velocity, but it could not reproduce the high-velocity components at the innermost radii. In contrast, a simulation with a higher mass requires the smaller inner radii and larger outer radii to fit the observed rotation curve. However, we cannot exclude the possibility of the higher central mass because we did not consider the offset from the disk midplane and the effect of the outflow. Also, it is possible that the spatial resolution and sensitivity of our observation was not enough to detect the detailed structure near the inner and outer radii. Thus, we notice again that the mass of $7M_{\odot}$ is a lower limit of the mass of Source I.

The estimated mass of $7M_{\odot}$ is consistent with those derived by Plambeck & Wright (2016) and Hirota et al. (2014), as well as the mass estimated with 43 GHz SiO masers (Matthews et al. 2010). The velocity gradient of the $v=1$ and 2 SiO masers supports the rotating structure with the enclosed mass of $\sim 7-8M_{\odot}$ (Kim et al. 2008; Matthews et al. 2010). The rotation curve of 336 GHz H_2O and 340 GHz molecular lines also suggest the rotating ring with the central mass of $\sim 5-7M_{\odot}$.

(Hirota et al. 2014; Plambeck & Wright 2016). Also, Hirota et al. (2017) suggested the mass of Source I to be $8.7M_{\odot}$ with the rotation of the $\text{Si}^{18}\text{O } J=12-11$ emission.

On the other hand, recent ALMA observation with the resolution $< 0.06''$ detected 232 GHz H_2O line tracing the X-shape distribution of $\text{SiO } v=1$ and $2 J=1-0$ masers (Ginsburg et al. 2018). Using the outer edge of the position-velocity diagram, they estimated a mass of Source I of $> 15 \pm 2 M_{\odot}$, which is twice of the previous estimations and the result of this observation. This inconsistency could be caused by the fact that we missed a faint emission at high-velocity component near the central source due to the insufficient resolution and sensitivity. Also, because our model based on the emission centroids samples only the peak positions at the position-velocity diagram, it gives the lower mass compared with the case using the highest velocity at a certain position as Ginsburg et al. (2018) does.

Figure 4 (a) displays the position-velocity diagram of the $\text{SiO } v=4 J=11-10$ emission. We could not fit the data with the Keplerian rotation curve because the power-law profile is not clear in our PV diagram, so we overlaid the Keplerian velocity curve for 10 and $15M_{\odot}$. It also shows the possibility that the estimated mass can be modified if we can confine the velocity structure more precisely. The future observations with the higher resolution and sensitivity are required to constrain the central mass with the kinematics in this scale.

Although the resolution of our observation is not enough to resolve the issue on the mass estimation of Source I, our observation shows that the $\text{SiO } v=4 J=11-10$ emission traces the small region with radius < 30 AU tracing the disk surface and the inner outflow. Their high excitation level and the compact distribution implies that $\text{SiO } v=4 J=11-10$ emission is a promising tracer to study the kinematics of the innermost region where the outflow is launching with the higher resolution observations in the future.

4.3. Summary

We observed SiO line around Source I with a resolution of $\sim 0.1''$ and found the following:

1. We detected $\text{SiO } v=4 J=11-10$ line near Source I. This is the first detection of $\text{SiO } v=4$ emission in the star-forming regions. Besides, the nature of the emission enables us to trace the inner part of the disk/outflow system of Source I using observations with higher resolution in the future.
2. $\text{SiO } v=2 J=10-9$ emission shows the bipolar distribution with a size of $0.5'' \times 0.5''$, tracing the base of the northeast-southwest outflow from Source I. While, $^{29}\text{SiO } v=2$ and $\text{SiO } v=4 J=11-10$ line show the compact distribution tracing the surface of the disk and the base of the outflow of Source I.
3. The centroids of the velocity distribution of $\text{SiO } v=4 J=11-10$ line suggest that the emission traces the ring structure with $12 \text{ AU} < r < 26 \text{ AU}$ and the central mass of $7M_{\odot}$. The estimated value would be a lower limit of the mass because the sensitivity and resolution of our observation are not enough to resolve the faint components in the rotation curve.

This paper makes use of the following ALMA data: ADS/JAO.ALMA#2013.1.00048.S. ALMA is a partnership of ESO (representing its member states), NSF (USA) and NINS (Japan), together with NRC (Canada), NSC and ASIAA (Taiwan), and KASI (Republic of Korea), in cooperation with the Republic of Chile. The Joint ALMA Observatory is operated by ESO, AUI/NRAO and NAOJ. We thank the staff at ALMA for making observations and reducing the data. TH is financially supported by the MEXT/JSPS KAKENHI Grant Numbers 24684011, 16K05293, 17K05398, and 18H05222. KM is supported by the MEXT/JSPS KAKENHI Grant Number 15K17613. MH is supported by the MEXT/JSPS KAKENHI Grant Numbers 24540242 and 25120007. Data analysis were in part carried out on common use data analysis computer system at the Astronomy Data Center, ADC, of NAOJ.

Facilities: ALMA.

REFERENCES

- Bally, J., Cunningham, N. J., Moeckel, N., et al. 2011, *ApJ*, 727, 113
- Cernicharo, J., Bujarrabal, V., & Santaren, J. L. 1993, *ApJ*, 407, L33
- Chatterjee, S., & Tan, J. C. 2012, *ApJ*, 754, 152
- Decin, L., Richards, A. M. S., Danilovich, T., Homan, W. & Nuth, J. A. 2018, arXiv e-prints, 1801.09291
- Ginsburg, A., Bally, J., Goddi, C., Plambeck, R. & Wright, M. 2018, *ApJ*, 860, 119
- Goddi, C., Greenhill, L. J., Chandler, C. J., et al. 2009, *ApJ*, 698, 1165
- Goddi, C., Humphreys, E. M. L., Greenhill, L. J., Chandler, C. J., & Matthews, L. D. 2011, *ApJ*, 728, 15
- Greenhill, L. J., Gwinn, C. R., Schwartz, C., et al. 1998, *Nature*, 396, 650
- Greenhill, L. J., Goddi, C., Chandler, C. J., Matthews, L. D., & Humphreys, E. M. L. 2013, *ApJ*, 770, 32
- Hirota, T., Bushimata, T., Choi, Y. K., et al. 2007, *PASJ*, 59, 897
- Hirota, T., Kim, M. K., Honma, M. 2012, *ApJ*, 757, L1
- Hirota, T., Kim, M. K., Kurono, Y., & Honma, M. 2014, *ApJ*, 782, L28
- Hirota, T., Kim, M. K., Kurono, Y. & Honma, M. 2015, *ApJ*, 801, 82H

- Hirota, T., Kim, M. K., & Honma, M. 2016a, *ApJ*, 817, 168
- Hirota, T., Machida, M. N., Matsushita, Y., et al. 2016b, *ApJ*, 833, 238
- Hirota, T., Machida, M. N., Matsushita, Y., et al. 2017, *Nature Astronomy*, 1, 146
- Issaoun, S., Goddi, C., Matthews, L. D., et al. 2017, *A&A*, 606, 126
- Kervella, P., Decin, L., Richards, A. M. S. et al. 2018, *A&A*, 609, 67
- Kim, M. K., Hirota, T., Honma, M., et al. 2008, *PASJ*, 60, 991
- Kleinmann, D. E. & Low, F. J. 1967, *ApJ*, 149, L1
- Luhman, K. L., Robberto, M., Tan, J. C., et al. 2017, *ApJ*, 838, 3
- Matthews, L. D., Greenhill, L. J., Goddi, C., et al. 2010, *ApJ*, 708, 80
- Menten, K. M., Reid, M. J., Forbrich, J., & Brunthaler, A. 2007, *A&A*, 474, 515
- Niederhofer, F., Humphreys, E. M. L., & Goddi, C. 2012, *A&A*, 548, A69
- Müller, H. S. P., Schlöder, F., Stutzki, J., & Winnewisser, G., 2005, *J. Mol. Struct.*, 742, 215
- Orozco-Aguilera, M. T., Zapata, L. A., Hirota, T., Qin, S.-L. & Masqué, J. M. 2017, *ApJ*, 847, 660
- Plambeck, R. L., Wright, M. C. H., & Carlstrom, J. E. 1990, *ApJ*, 348, L65
- Plambeck, R. L., Wright, M. C. H., Friedel, D. N., et al. 2009, *ApJ*, 704, L25
- Plambeck, R. L. & Wright, M. C. H. 2016, *ApJ*, 833, 219
- Reid, M. J., Menten, K. M., Greenhill, L. J., & Chandler, C. J. 2007, *ApJ*, 664, 950
- Rodríguez, L. F., Poveda, A., Lizano, S., & Allen, C., 2005, *ApJ*, 627, 65
- Rodríguez, L. F., Dzib, S. A., Loinard, L., et al. 2017, *ApJ*, 140, 8
- Vaidya, B. & Goddi, C. 2013, *MNRAS*, 429, 50
- Wright, M. C. H., Plambeck, R. L., & Wilner, D. J. 1996, *ApJ*, 469, 216
- Wu, Y., Liu, T., & Qin, S. 2014, *ApJ*, 791, 123
- Zapata, L. A., Rodríguez, L. F., Schmid-Burgk, J., et al. 2012, *ApJ*, 745, L17